Electronics **2015**, *4*, 947-968; doi:10.3390/electronics4040947

OPEN ACCESS

electronics

ISSN 2079-9292

www.mdpi.com/journal/electronics

Article

A Technique for Mitigating Thermal Stress and Extending Life Cycle of Power Electronic Converters Used for Wind Turbines

Canras Batunlu and Alhussein Albarbar *

School of Engineering, Manchester Metropolitan University, M1 5GD, Manchester, UK;
E-Mail: canras.batunlu@stu.mmu.ac.uk

***** Author to whom correspondence should be addressed; E-Mail: a.albarbar@mmu.ac.uk;
Tel.: +44-0161-247-6297; Fax: +44-0161-247-6297.

Academic Editor: Mostafa Bassiounis

Received: 21 September 2015 / Accepted: 10 November 2015 / Published: 17 November 2015

Abstract: Over the last two decades, various models have been developed to assess and improve the reliability of power electronic conversion systems (PECs) with a focus on those used for wind turbines. However, only few studies have dealt with mitigating the PECs thermo-mechanical effects on their reliability taking into account variations in wind characteristics. This work critically investigates this issue and attempts to offer a mitigating technique by, first, developing realistic full scale (FS) and partial scale (PS) induction generator models combined with two level back-to-back PECs. Subsequently, deriving a driving algorithm, which reduces PEC's operating temperature by controlling its switching patterns. The developed switching procedure ensures minimum temperature fluctuations by adapting the variable DC link and system's frequency of operation. It was found for both FS and PS topologies, that the generator side converters have higher mean junction temperatures where the grid side ones have more fluctuations on their thermal profile. The FS and PS cycling temperatures were reduced by 12 °C and 5 °C, respectively. Moreover, this led to a significant improvement in stress; approximately 27 MPa stress reduction for the FS induction generator PEC.

Keywords: insulated gate bipolar transistor (IGBT); thermo-mechanical FE analysis; PWM control; wind energy converter model; thermal management; dynamic DC link

---

1. Introduction

Wind energy converters (WECs) have become one of the fastest developing renewable energy technologies. The performance and life cycle of WECs highly depend on power electronic converters (PECs). PECs play vital roles in conditioning the harvested energy and in interfacing with utility grids. However they suffer from reliability related issues caused by variable and unpredictable wind and other natural effects [1,2]. Due to their ease of driving and higher frequency switching capacities compared to other semiconductor devices, insulated gate bipolar transistors (IGBTs) found their wide applications in PECs. Malfunctions of PECs cause failures to electrical/control systems within WECs and contribute to approximately 41% of the total causes [3]. Temperature is one of the common causes and responsible for about 60% of PECs failures [4]. Temperature fluctuations lead to degradation in bonded adjacent layers of these semiconductor devices and eventual failures occur due to the thermal expansion. In literature, various analytical models has been proposed [5–9] to solve heat transfer through PECs. Electro thermal models for an IGBT based half bridge [10], two level back-to back [11] and for multi-level PECs [12,13] have also been developed.

PECs are divided into two categories in wind energy systems, partial scale (PS) and full scale (FS), where doubly fed induction generator (DFIG) is common option for PS topology as seen in Figure 1. Senturk *et al.* [14] studied a thermal power capability determination algorithm for different multilevel topologies consist of press-pack IGBTs of grid side FS converter. Blaabjerg *et al.* [15] presented another case study on WECs for providing life time prediction and temperature cycling analysis. DC link voltage adaption is also one of the promising choices for WECs in terms of reliability and life time extension. In renewables such as solar [16,17] or wind [18,19] systems, controlling the DC bus voltage is already important for maximum power point tracking (MPPT), avoiding distorted energy generation and grid interfacing. El-Sousy *et al.* [20] studied a DC link voltage regulation model for a grid connected FS wind system in order to provide a MPPT technique. Bekakra and Attous [21] also developed a DC link voltage control method for a DFIG based back-to back converter connected to a variable speed wind turbine. In these control strategies the main aim is to keep DC voltage steady. However, it is also possible to operate these systems with dynamic DC link voltage as discussed by Dayarante *et al.* [22]. Lower DC link voltage can decrease the power losses [22,23]. However, it would also cause large fluctuation and hence larger thermal in the grid side converters. Especially, this should be avoided at low switching frequencies for protecting the utility grid inverter from highly distorted AC signals. Monitoring the DC link current and voltage ripple analysis proposed by Pei *et al.* [24] or constrained optimal current control adoption method studied by Lemmens *et al.* [25] can be two options for protecting the generator side converter from such worse case scenarios. However, based on the grid power requirements, operating at constant switching frequency would cause higher switching losses due to the higher current injection to grid side if DC link voltage is not sufficient. Therefore, controlling the switching frequency becomes crucial for the dynamic DC link voltage adaption methods. Recently, Andresen and Liserre [26] analysed the thermal cycles of the junction temperature in dependence of current and switching frequency and they derived a switching utilization method for an electrical vehicle by using space vector modulation (SVM).

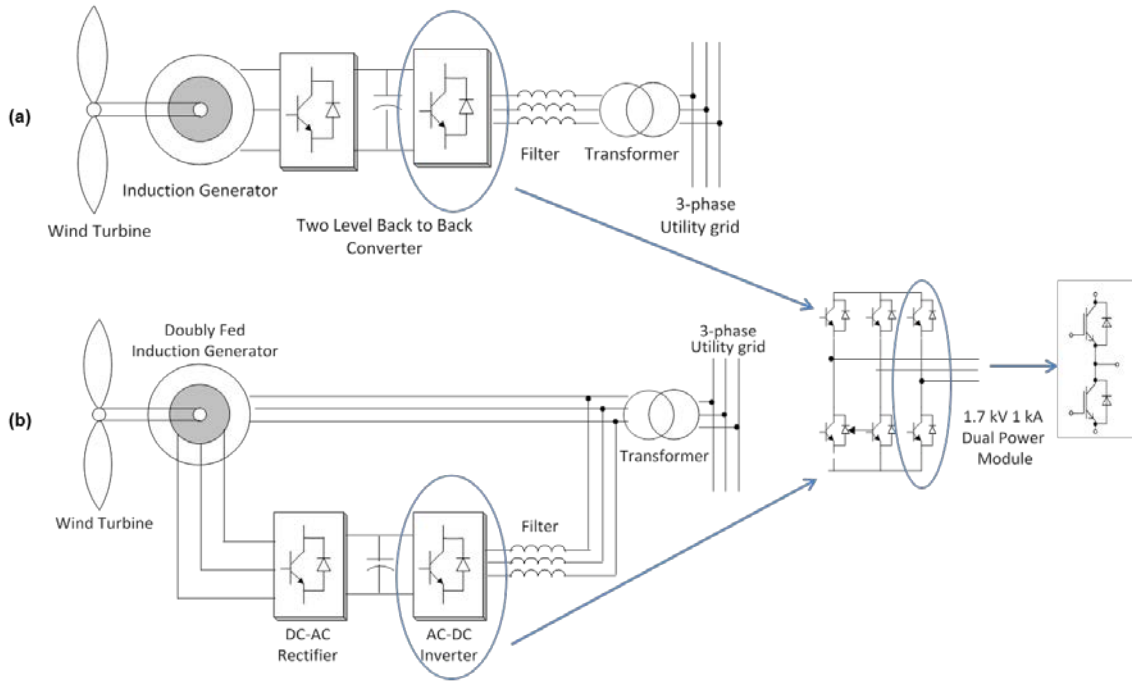

Figure 1. Two level back-to-back converter topology in (**a**) full scale (FS) and (**b**) partial scale (PS) based wind energy system.

Based on the surveyed research work, there is still a need for an accurate IGBT model to understand its thermal characteristics under wide wind speed variations. Thermally induced effects, e.g., thermal stress caused by temperature fluctuations, of the dynamic DC link operation have not been thoroughly analysed in literature. This paper offers a new switching frequency driving scheme, based on the optimised DC link voltage requirements. A conventional 1.7 kV/1 kA dual IGBT power electronic module, as shown in Figure 1, was used to build the PEC of the wind energy system in Simulink. The developed scheme was embedded in power loss models to minimise temperature fluctuations. The performance of the proposed scheme was validated and compared with the conventional back-to-back topology based constant and dynamic DC link operations. A finite element model (FEM) combined with a Simulink code was established to monitor PECs thermally induced stress based on the estimated actual power loss profiles for different topologies. The paper starts by investigating PEC's heat generating sources in Section 2, as well as describing dynamic DC link voltage control and proposed switching frequency adjusting technique. In Section 3, critical assessment of the proposed control scheme is demonstrated and results are compared with the performance of conventional methods. Conclusions are depicted in final Section of the paper.

2. State of the Art Electro-Thermal Model of IGBT Power Module

2.1. Power Loss Modelling

Developing a proper electro thermal model strictly requires effective power loss calculation and integration of the heat generation represented by internal self-heating and cross coupling effects of diode chips as well as the IGBTs. During recovery operation, heat generation occurs among neighbour and adjacent layers due to the reverse current over diode chips which also affect the mean junction

temperature. Power losses in PECs used for wind applications are described schematically in Figure 2. The stepper change in *di*/*dt* and *dv*/*dt* causes the total switching losses which leads to increase in the temperature through the device. Switching energy losses for a single power electronics module, over one period of switching processes, are divided into Turn-on and Turn-off losses, $E_{SW,ON}$ and $E_{SW,OFF}$, for the IGBT. The instantaneous switching power losses, $P_{SW,IGBT}$ of IGBT can be calculated as [27,28]:

$$P_{SW,IGBT}(t) = f_S.\left(E_{SW,ON}(I_C(t))+E_{SW,OFF}(I_C(t))\right) \quad (1)$$

where I_c is the IGBT collector current and f_s is the switching frequency. The average switching power loss of IGBTs, $P_{SW,IGBTAV}$ can be expressed as the integral of instantaneous power losses as:

$$P_{SW,IGBTAV} = f_o f_S \int_0^{1/f_o} \left(E_{SW,ON}(I_C(t))+E_{SW,OFF}(I_C(t))\right)dt \quad (2)$$

where f_o is the fundamental frequency. Similarly, diode instantaneous recovery power losses, $P_{SW,DIODE}$, can be denoted by means of recovery energy, $E_{SW,RR}$, as:

$$P_{SW,DIODE}(t) = f_S.E_{SW,RR}(I_F(t)) \quad (3)$$

where I_F is the forward current across the diodes. Average recovery power loss then can be derived as:

$$P_{SW,DIODEAV} = f_o f_S \int_0^{1/f_o} \left(E_{SW,RR}(I_F(t))\right)dt \quad (4)$$

Average switching power losses, $P_{SW,AV}$, over IGBT and diodes within total number of cycle, N, in each fundamental frequency at n^{th} switching period can be denoted as [2,28]:

$$P_{SW,AV} = f_o \sum_{n=1}^{N}\left[E_{SW,ON}(I_C(n))+E_{SW,OFF}(I_C(n))+E_{SW,RR}(I_F(n))\right] \quad (5)$$

Total conduction loss of power module is composed of the total IGBT/diode chips conduction losses, $P_{CON,IGBT}$ and $P_{CON,DIODE}$, respectively. The instantaneous conduction loss, P_{CON} can be derived as:

$$P_{CON}(t) = P_{CON,IGBT}(t) + P_{CON,DIODE}(t) = V_{CE}(I_C(t)).I_C(t).D_I(t) + V_F(I_F(t)).I_F(t).D_D(t) \quad (6)$$

where, V_{CE} is the collector-emitter saturation voltage of the IGBT. V_f and I_f are the forward conduction voltage and current of the diode, respectively. D_I is the conduction time of the IGBTs and D_D for the diodes. Average conduction power loss, $P_{CON,AV}$ can be expressed as the integral of instantaneous power losses as [2–28]:

$$P_{CON,AV} = f_o \int_0^{1/f_o} P_{CON}(t)dt = f_o \int_0^{1/f_o} \left[V_{CE}(I_C(t)).I_C(t).D_I(t)+V_F(I_F(t)).I_F(t).D_D(t)\right]dt \quad (7)$$

Average switching power losses, $P_{CON,AV}$, over IGBT and diodes within total number of cycle, can be derived as:

$$P_{CON,AV} = f_o \sum_{n=1}^{N} [V_{CE}(I_C(n)).I_C(n).D_I(n) + V_F(I_F(n)).I_F(n).D_D(n)] \quad (8)$$

In this study, overall switching and conduction power losses were calculated by a datasheet study and stored in look up tables (LUTs) for each chip [29]. LUTs interpolate the energy losses based on the defined current characteristics of each chip with respect to the instantaneous temperature. Switching power loss calculation is triggered by edge detector before and after the condition duration for each IGBT/Diode.

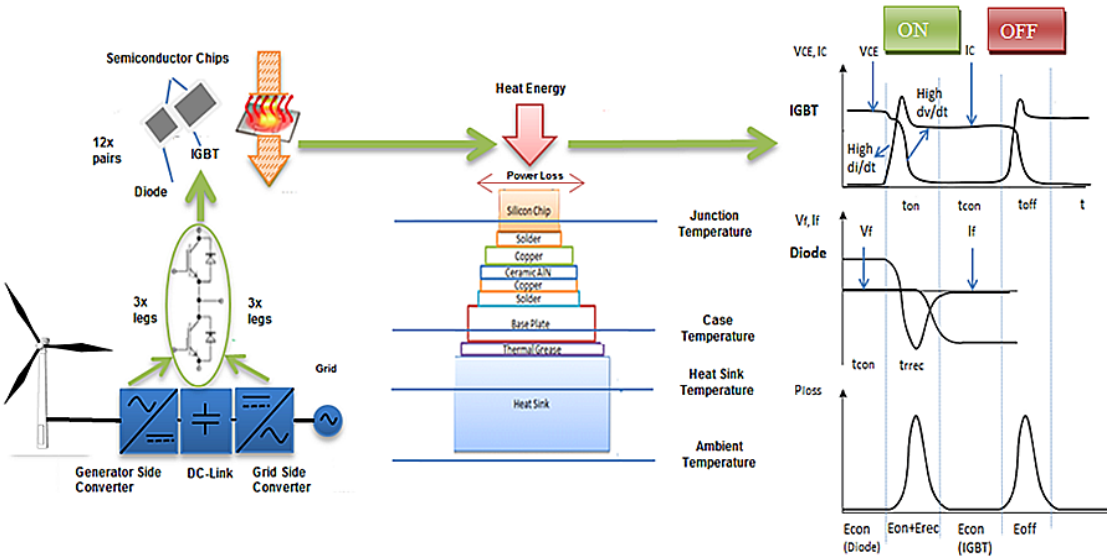

Figure 2. Power loss characteristics of power electronic conversion systems (PECs) in wind applications (modified from [29], Copyright 2009, IEEE).

2.2. 3-D Finite Element Modelling

An IGBT module attached to a heat sink was modelled using 3-D FEM as seen Figure 3a, based on the actual dimensions and the material properties stated in Table 1. The heat distribution through each material was generated using Equation (9):

$$\frac{\partial^2 T}{\partial x^2} + \frac{\partial^2 T}{\partial y^2} + \frac{\partial^2 T}{\partial z^2} + \frac{q}{k} = \frac{\rho.c}{k} \frac{\partial T}{\partial t} \quad (9)$$

where T is the temperature, k is the thermal conductivity, c is specific heat capacity, ρ is the mass density and q is the rate of generation of energy per unit volume. Material properties such as conductivity or coefficient of thermal expansion are temperature dependent.

Physical material properties are therefore defined as dynamic properties and as function of temperature as shown in Figure 3b e.g., for silicon layer. Two cylindrical domains, representing liquid cooling elements, are placed across the heat sink, operated at 25 °C. Bottom surface was modelled as convection boundary, where heat transfer coefficient h is found as 4200 W/m^2·K using Equation (10):

$$h = R_{th,hs}.A_{hs} \tag{10}$$

where A_{hs} is the surface area and $R_{th,hs}$ is the thermal resistance of the heat sink.

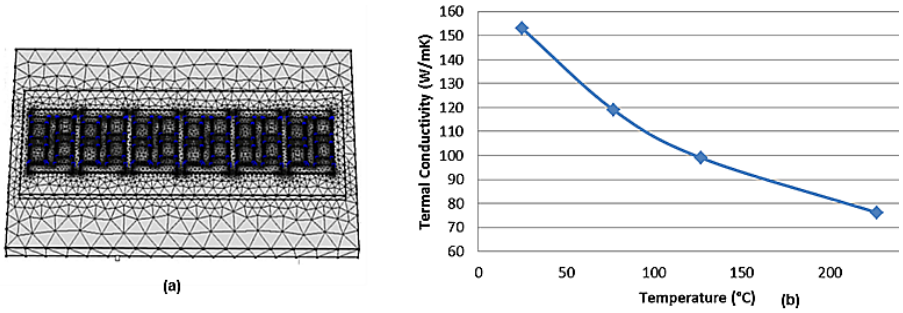

Figure 3. (**a**) Meshed model view (**b**) dynamic thermal conductivity property of silicon layer.

Table 1. Physical properties of each layer material at 25 °C [29–32].

Layer	Physical Properties at 25 °C					
	ρ (kg/m^3)	K (W/m·K)	c (J/(kg·K)	CTE (10^{-6}/K)	Young Modulus (MPa)	Poisson Ratio
Silicon	2330	153	703	3.61	113.000	0.28
Solder	7360	33	200	30.20	27.557	0.40
Copper	8850	398	380	17.30	128.000	0.36
Aluminium	3300	180	750	4.60	344.000	0.22
Copper	8850	398	380	17.30	128.000	0.36
Solder	11,300	35	129	29	16.876	0.44
Baseplate	3010	180	741	0.27	192.000	0.24
T. Grease	2500	2	700	29	15.700	0.32
Heat Sink	2730	155	893	4.30	384.000	0.30

Thermal grease between heat sink and base plate was defined as boundary with 2 W/m·K conductivity. Initially, a constant 200 W heat was applied in time domain on each chip located on the module where the initial temperature was 25 °C. In order to generate thermal network, simulation was computed until the step response of heating curve reaches steady state as seen in Figure 4a,b. Thermal resistance R_{th} and capacitance C_{th} for each individual layer were extracted by curve fitting using least square method; see Figure 4b. The thermal matrix, in Laplace domain, was then generated based on the self and coupling heating across [29] each active device by [33,34]:

$$T_m(s) = \sum_{n=1}^{N} \sum_{k=1}^{Kmn} \frac{A_{mnk}}{s+\alpha_{mnk}} P_n(s) \tag{11}$$

where P is the initial heat source, A is the coefficient $1/_{Cth}$ and α is the $1/\tau$. Temperature of each layer was represented for m layers and n heating sources. A matrix form of Equation (11) was derived as in Equation (12) where a_{12}, … a_{MN} are the transfer functions of thermal impedances [33,34].

$$\begin{bmatrix} T_{j1} \\ T_{j2} \\ \vdots \\ T_{jN} \\ T_{solder1} \\ \vdots \\ T_{AlNN} \\ \vdots \\ T_{baseplate} \end{bmatrix} = \begin{bmatrix} a_{11} & a_{12} & \cdots & a_{1N} \\ a_{21} & a_{22} & \cdots & a_{2N} \\ & \vdots & \vdots & \\ a_{N1} & a_{N2} & \cdots & a_{NN} \\ & \vdots & & \\ & \vdots & & \\ & \vdots & & \\ a_{M1} & a_{M2} & & a_{MN} \end{bmatrix} \cdot \begin{bmatrix} P_{in1} \\ P_{in2} \\ \vdots \\ P_{inN} \end{bmatrix} + T_0 \quad (12)$$

By applying Forward Rectangular Euler's rule, the thermal equation is converted in z-domain [29] to increase computational efficiency in Simulink. It can be written as:

$$\Delta T = \frac{P_i}{C_{th}} \frac{1}{z-1} - \frac{\Delta T}{R_{th}C_{th}} \frac{1}{z-1} \quad (13)$$

Look up tables were used to interpolate the previously defined energy losses as function of device current, saturation voltage and temperature. Simulink blocks were used to generate thermal impedance equivalence defined in Equation (13) integrated within previously defined self and coupling heating based thermal impedances for all IGBT/diode chips and all layers underneath. The transient temperature was obtained by processing transient power losses as input to thermal models as a function of transient temperature which is the output of thermal models across each chip.

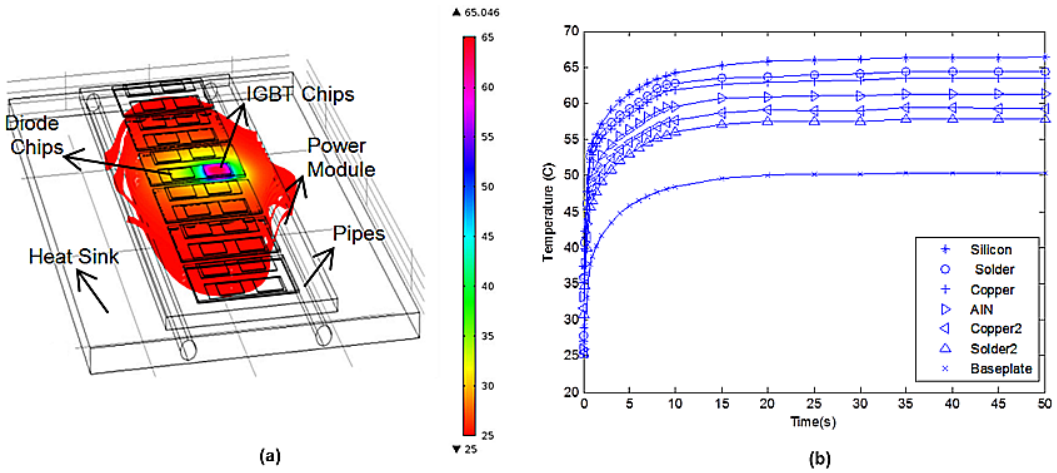

Figure 4. (**a**) Temperature distribution due to heating (**b**) layer temperature and fitted data.

The mismatch among adjacent layers of the module is non uniform due to the coefficient of thermal expansions (CTE) differences of each material [35,36]. This generates thermally induced stress which causes deformation and eventual solder delamination and bond-wire lift off based on the stored elastic energy. In order to present stress-strain and maximum stress (von Misses) distribution, FE model was subjected to the power loss profile extracted from each three different operations of wind energy system models, stated in introduction section. In the FE model, the stress distribution was defined by the yield function F as:

$$F = \sigma_{mises} - \sigma_{yield} \tag{14}$$

where σ_{yield} is the yield stress and σ_{mises} is the von Mises stress. It is derived from the deviatoric stress tensor, which consider the stress due to the shape changes and is given as:

$$\sigma_{mises} = \sqrt{\frac{3}{2} dev(\sigma) : dev(\sigma)} \tag{15}$$

It is used in failure tests such as in [35] where the maximum von Mises stress should be less than the yield strength in such operations. Anand's model [37] was also used to describe the solder layers behaviour such as temperature sensitivity as described in [36].

2.3. Wind Turbine and Utility Grid Modelling

FS and PS based two level back-to-back (BTB) power converter topologies were modelled individually with an induction generator based wind turbine system model in Simulink. Wind turbine converted mechanical output power is described by Equation (16):

$$P_m = c_p(\lambda, \beta) \frac{\rho A}{2} v_{wind}^3 \tag{16}$$

where P_m is the mechanical output power, c_p is the performance coefficient of the turbine, ρ is the air density, A is the turbine swept area, v_{wind} is the wind speed, λ is the tip speed ratio of the rotor blade to wind speed and β is the pitch angle.

The base wind speed of the turbine model is 12 m/s and nominal output power is 1.5 MW. Simulated power characteristic of turbine with respect to speed and output power is seen in Figure 5.

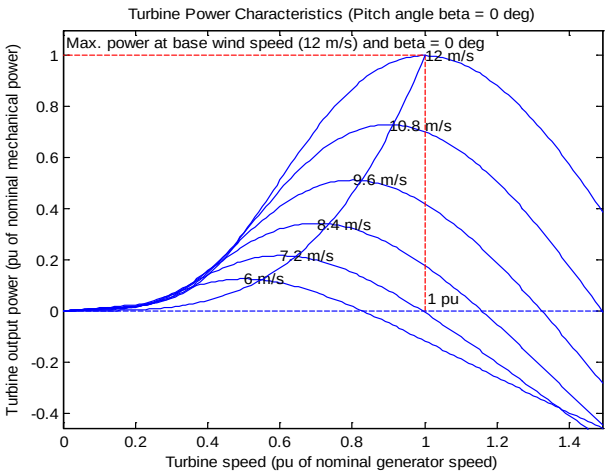

Figure 5. Wind turbine characteristics and power-speed curve.

2.4. DC Link Voltage Regulation and Grid Side Converter Control

The control for both grid and generator converters was assessed by sinusoidal pulse width modulation method (SPWM). Equivalent voltage equation in a balanced grid connected to a three phase PWM converter through a filter branch is given as [38,39]:

$$v_L = v_f + v_C \tag{17}$$

where converter voltage v_c, filter voltage v_f, line resistance R and inductance L are formed as:

$$v_L = Ri_L + L\frac{di_L}{dt} + v_C \tag{18}$$

R can be neglected since it has much lower voltage drop than L and the three-phase voltages ($v_{a,b,c}$) can be represented with respect to line currents ($i_{a,b,c}$) and converter voltages ($v_{ca,b,c}$)as:

$$\begin{bmatrix} v_a \\ v_b \\ v_c \end{bmatrix} = L\frac{d}{dt}\begin{bmatrix} i_a \\ i_b \\ i_c \end{bmatrix} + \begin{bmatrix} v_{Ca} \\ v_{Cb} \\ v_{Cc} \end{bmatrix} \tag{19}$$

The equivalence of Equation (19) in α-β stationary coordinates becomes:

$$\begin{bmatrix} v_{L\alpha} \\ v_{L\beta} \end{bmatrix} = L\frac{d}{dt}\begin{bmatrix} i_{L\alpha} \\ i_{L\beta} \end{bmatrix} + \begin{bmatrix} v_{C\alpha} \\ v_{C\beta} \end{bmatrix} \tag{20}$$

Then Equation (20) is represented in rotating *d-q* frame as:

$$v_{Ld} = L\frac{di_{Ld}}{dt} - \omega L i_{Lq} + v_{Cd} \tag{21}$$

$$v_{Lq} = L\frac{di_{Lq}}{dt} + \omega L i_{Ld} + v_{Cq} \tag{22}$$

where ω is the angular frequency. As discussed in [39], usage of trigonometrical relation leads to define boundary condition by using Equations (21) and (22) as:

$$\left| v_{Ldq} - j\omega L i_{Ldq} \right| = \frac{\sqrt{3}}{2} v_{Cdq} \tag{23}$$

Assuming $v_{Cdq} = \frac{2}{3}V_{dc}$, $V_{Ldq} = E_m$, where E_m is voltage amplitude, when only active power is supplied to the grid which leads $i_{Ldq} = i_{Ld}$, minimum DC-Link voltage boundary is defined as:

$$v_{dclink} > \sqrt{3E_m^2 + (\omega L i_{Ld})^2} \tag{24}$$

Based on the minimum DC-link voltage, PWM signals are synchronised with the grid voltage by zero detection scheme. I_q represents the reactive power component and hence it is desirable to be zero. Whereas, the desired magnitude for I_d, depends on actual voltage measured across the DC link. The converter output voltages V_{cd} and V_{cq} were regulated based on the difference between measured and reference values of the *d-q* current. Hence magnitude and phase angle delay of converter output voltages corresponding to grid voltages are set by:

$$v_{L(pk)} = \sqrt{V_{cd}^2 + V_{cq}^2} \tag{25}$$

$$\theta = \tan^{-1}\frac{V_{cq}}{V_{cd}} \tag{26}$$

2.5. Generator Side Control with Switching Frequency Regulation

Similar to the derived *d-q* elements for the three phase line voltages in previous section, stator voltages $v_{sd,q}$ can be expressed as follows [38,39]:

$$v_{sd} = R_s i_{sd} + \frac{d}{dt}\lambda_{sd} - w_d \lambda_{sq} \tag{27}$$

$$v_{sq} = R_s i_{sq} - \frac{d}{dt}\lambda_{sq} + w_d \lambda_{sd} \tag{28}$$

where ω_d is instantaneous speed of *d-q* winding set in the air gap, $\lambda_{sd,q}$ and $\lambda_{rd,q}$ are the stator and rotor flux linkage expressions, respectively. $v_{rd,q}$ rotor winding voltages are given as:

$$v_{rd} = R_r i_{rd} + \frac{d}{dt}\lambda_{rd} - w_{dA}\lambda_{rq} \tag{29}$$

$$v_{rq} = R_r i_{rq} + \frac{d}{dt}\lambda_{rq} + w_{dA}\lambda_{rd} \tag{30}$$

where ω_{dA} is the instantaneous speed of the *d-q* winding set in the air gap with respect to the rotor *A*-axis speed. The relation between inductances can be defined a unit less term leakage factor, σ as:

$$\sigma = 1 - \frac{L_m^{\,2}}{L_s L_r} \tag{31}$$

where L_s and L_r are the stator and rotor inductances and L_m is the magnetization inductance. Hence, the stator windings are defined as:

$$\lambda_{sd} = \sigma L_s i_{sd} + \frac{L_m}{L_r}\lambda_{rd} \tag{32}$$

$$\lambda_{sq} = \sigma L_s i_{sq} \tag{33}$$

Then, the stator *d-q* voltages can be expressed in terms of control and compensation terms as:

$$v_{sd} = \underbrace{R_s i_{sd} + \sigma L_s \frac{d}{dt} i_{sd}}_{v_{sd}'} + \underbrace{\frac{L_m}{L_r}\frac{d}{dt}\lambda_{rd} - w_d \sigma L_s i_{sq}}_{v_{sd,comp}} \tag{34}$$

$$v_{sq} = \underbrace{R_s i_{sq} + \sigma L_s \frac{d}{dt} i_{sq}}_{v_{sq}'} + \underbrace{w_d \frac{L_m}{L_r}\lambda_{rd} + w_d \sigma L_s i_{sd}}_{v_{sq,comp}} \tag{35}$$

For the DFIG based partial scale PE control, Equations (34) and (35) are derived by Equations (29) and (30) for rotor voltages control. The *d-q* voltages can be used to derive equivalent stator generator voltage as:

$$v_s = \sqrt{\frac{3}{2}(v_{sd}^2 + v_{sq}^2)} \quad (36)$$

In steady state balanced conditions, it is equal to the line voltage, V_L, which can be defined in terms of DC link voltage as:

$$v_{L(rms)} = V_{dclink} \frac{\sqrt{3}}{2\sqrt{2}} \quad (37)$$

Then V_{dclink} in Equation (37) was defined as minimum value based on the generator voltage with respect to generator speed. The boundary has been rearranged as:

$$V_{dclink}(\min) > \frac{2\sqrt{2}}{\sqrt{3}} v_{LL(rms)} + \Delta V \quad (38)$$

where a control margin is set to $\Delta V = 10$ V. Look up tables are used to provide the mechanical torque with respect to reference speed. The mechanical power is also interpolated based on the power *vs.* speed characteristic derived in Figure 6. Reference stator *d-q* currents as well as the compensation elements of the stator voltages are also extracted through LUTs data obtained through Equations (32)–(35) by means of angular speed and power. The DC link voltage is adjusted to its minimum value in the DC link calculation block by LUTs during operation. It is derived based on the stored generator voltage and speed data obtained thorough Equations (37) and (38) for the generator side; and based on the grid voltage, active power component I_d and power factor data obtained thorough Equations (23) and (24) for the utility grid side. It is then assigned by a scheme according to interpolated value through both sides of PEC.

The schematic of the proposed switching frequency adaption is shown in Figure 6. In the grid side inverter, the process needs to be monitored in terms of current injection, to protect the switching elements against high power losses. When wind speed decreases and minimum DC link voltage regulation begins, the edge detector block stores the latest calculated power loss for both sides of the PEC. Then switching frequency regulation block is activated in order to reduce the switching losses. The switching frequency is decreased as the stored power loss is less than the one extracted from active power loss block. When wind speed increase, the switching frequency is adjusted according to loss characteristic, as well. The lowest possible operating switching frequency is 2 kHz to mitigate lifetime consumption within converters caused by power cycling load of switching frequency. In order to keep each three-phase voltages in symmetric, switching frequency is adjusted by the ratio of modulation and carrier frequencies (f_m & f_c) in multiple of three as stated in Equation (39).

$$\frac{f_c}{f_m} = 3k, (k \varepsilon N) \quad (39)$$

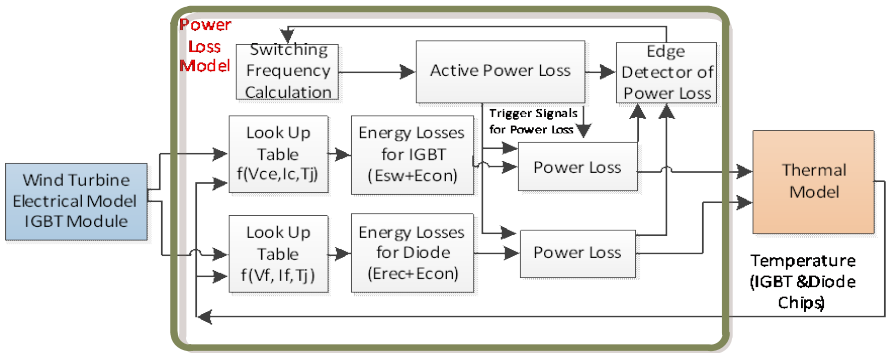

Figure 6. Schematic of the electro thermal model with switching frequency adaption.

3. Results and Discussion

3.1. Dynamic DC Link Voltage and Switching Frequency Analysis

The overall modules IGBT on time energy and conduction power losses are seen in Figure 7a,b, respectively. On time energy losses were expressed with respect to DC current and voltage at generator side converter (GSC) for different wind speeds as shown in Figure 7c. When wind speed is lower than the rated wind turbine speed, energy losses can be decreased by lowering the DC link voltage. For instance, approximately180 mJ loss deduction can be witnessed by reducing the DC link 50%, whilst keeping the current unchanged, when the wind speed is decreased from 12 m/s to 9 m/s.

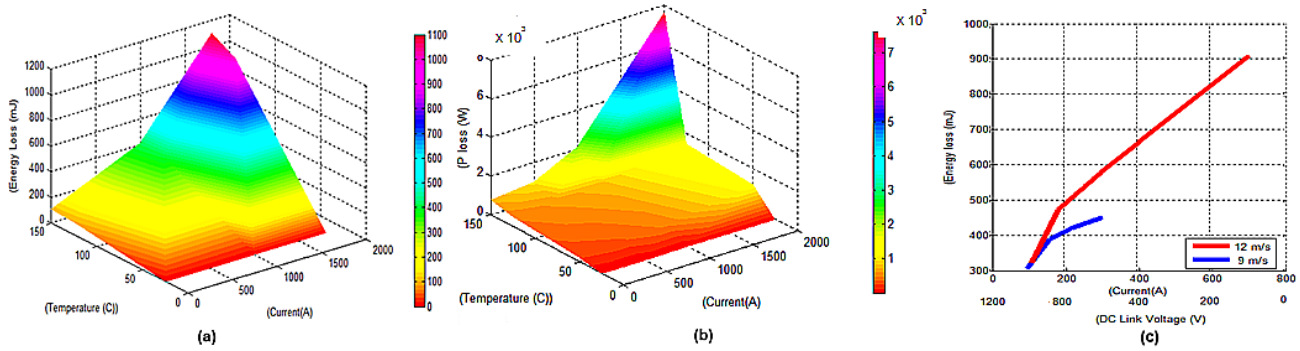

Figure 7. (**a**) Insulated gate bipolar transistor (IGBT) switching-on energy losses; (**b**) Conduction losses; (**c**) DC link voltage *vs.* current *vs.* on time losses.

Temperature fluctuations for the GSC with respect to current and switching frequency are shown in Figure 8a when the wind speed is 9 m/s. It can be seen that the temperature fluctuations can be kept constant by lowering the switching frequency around 50%, in the case approximately current increases 25%. Instantaneous on and off power losses, for instance, are found as 2.3 and 2.6 kW, respectively as seen in Figure 8b when switching frequency is 5 kHz. A case study is discussed for FS topology for expanding the switching frequency control without going into details. Figure 9a,b show a sample applied wind speed profile and the dynamic DC link operation for FS scheme grid side converter, respectively. The initial frequency is selected as 2 kHz where the DC link voltage is 650 V in the model.

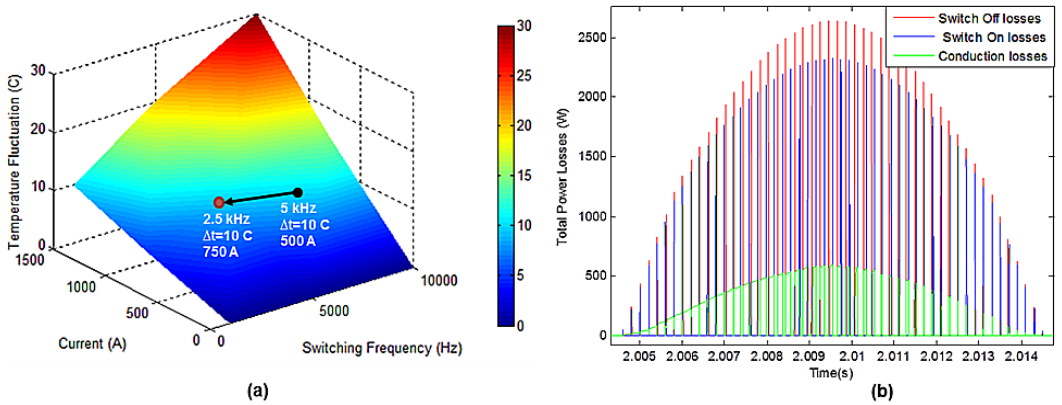

Figure 8. (**a**) Switching frequency effect during 9 m/s wind speed; (**b**) Total power losses at 5 kHz.

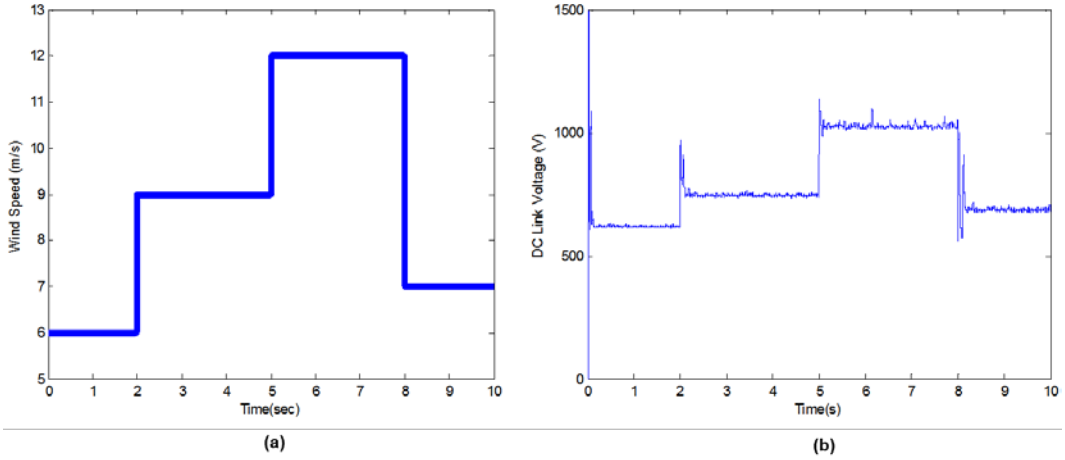

Figure 9. (**a**) Wind speed profile; (**b**) Adjusted DC link voltage.

At t = 2 s, wind speed is increased from 9 m/s to 12 m/s. The look up table which obtains minimum value for DC link operation is triggered and increases it to 748 V. At the meantime, the switching frequency is adjusted by the control block shown in Figure 6, in order to control switching loss for the assigned current and voltage through the power modules. It holds the latest calculated switching losses before the wind change detected by an edge detector and based on the next calculated power loss signal, the frequency is increased up to 2.55 kHz as shown in Figure 10a.

Similar operation also takes place at time t = 5 s and afterwards until t = 8 s. However at t = 8 s, a rapid power loss increase occurs due to higher current injection and frequency controller pulls switching frequency back by means of the ratio defined in Equation (33). The total power losses can also be seen in Figure 10b as the DC link voltage is controlled. Variable DC link and frequency operation causes fluctuation on the energy supplied to the utility grid. The three phase grid voltage can be seen in Figure 10c with distortion caused by the controller. Total harmonic distortion can also be illustrated in Figure 10d with respect to wind changes and switching frequency adjustments.

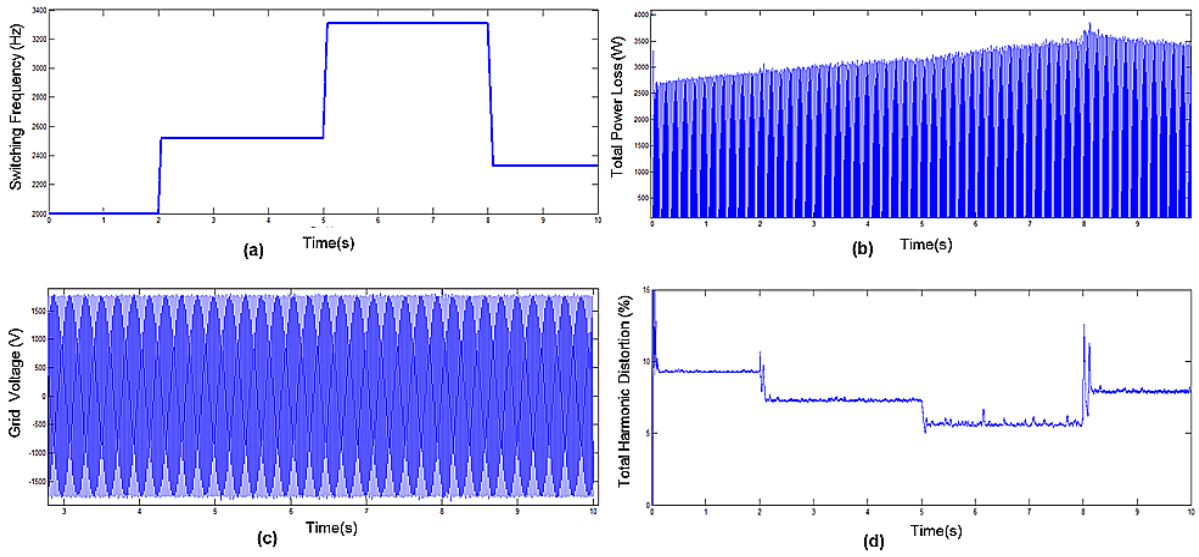

Figure 10. (**a**) Controlled power loss data by dynamic DC link and frequency operation; (**b**) Power losses; (**c**) Three phase grid voltage; (**d**) Total harmonic distortion.

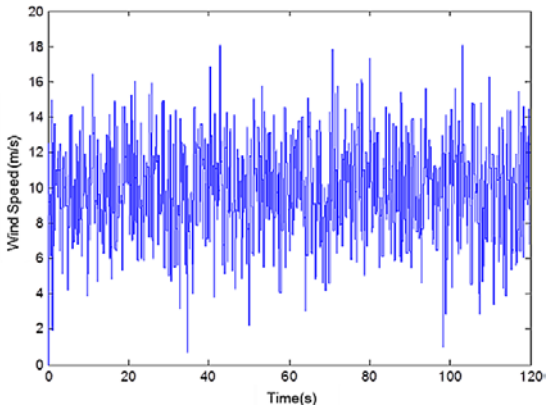

Figure 11. Applied wind speed profile.

Table 2. Thermal parameters extracted from the finite element model (FEM).

Layer	Thermal Capacitance			Thermal Resistance		
	$C_{th,1}$	$C_{th,2}$	$C_{th,3}$	$R_{th,1}$	$R_{th,2}$	$R_{th,3}$
Silicon	0.48	113.14	13.78	0.217	0.056	0.061
Solder	0.69	113.31	13.92	0.212	0.055	0.058
Copper	0.85	113.62	14.22	0.198	0.054	0.057
AIN	1.02	113.94	14.88	0.175	0.053	0.056
Copper	1.57	114.31	15.31	0.154	0.053	0.056
Solder	2.01	114.78	16.04	0.136	0.052	0.052
Baseplate	6.63	115.02	430.0	0.132	0.050	0.009

3.2. Comparison of Temperature Profiles for FS and PS Based Back to Back (BTB) PECs

A variable wind profile, shown in Figure 11, is applied both PS and FS models for determining the average junction temperature of IGBT chips. The simulation step time was 5 μs. Thermal parameters

for the central silicon chip (see Figure 5) and the layers underneath are shown in Table 2 which is obtained through FEM. In order to increase the accuracy, thermal impedances of each extracted curves were represented by three exponential terms. Thermal impedance for thermal grease layer is integrated within baseplate parameters since this layer was defined as a boundary for computational efficiency.

Temperature distributions for GSC and utility grid side (UGS) power modules in FS and PS based wind systems, in three different operation modes, are shown in Figures 12 and 13 respectively. As it is seen in Figure 12a, temperature distribution with a fixed DC link voltage (1.1 kV at 2.5 kHz) is much stable compare to the variable DC link operation (fixed at 2.5 kHz) shown in Figure 12b. Especially at wind speed below the rated shaft speed, the temperature fluctuation is higher. During static DC link operation, mean junction temperature is 92 °C where it is 80 °C for variable DC link operation. On the other hand, the junction temperature profile of the power module, when the proposed control scheme is applied (see Figure 12c), has less fluctuations compare to variable DC link operation. Lower mean junction temperature than with the one with static DC link voltage operation is also attained. It can also be seen than at lower wind speed (at t = 40 s), the temperature is higher compared to the dynamic DC link operation. This is due to the switching frequency increase controlled by the edge detector.

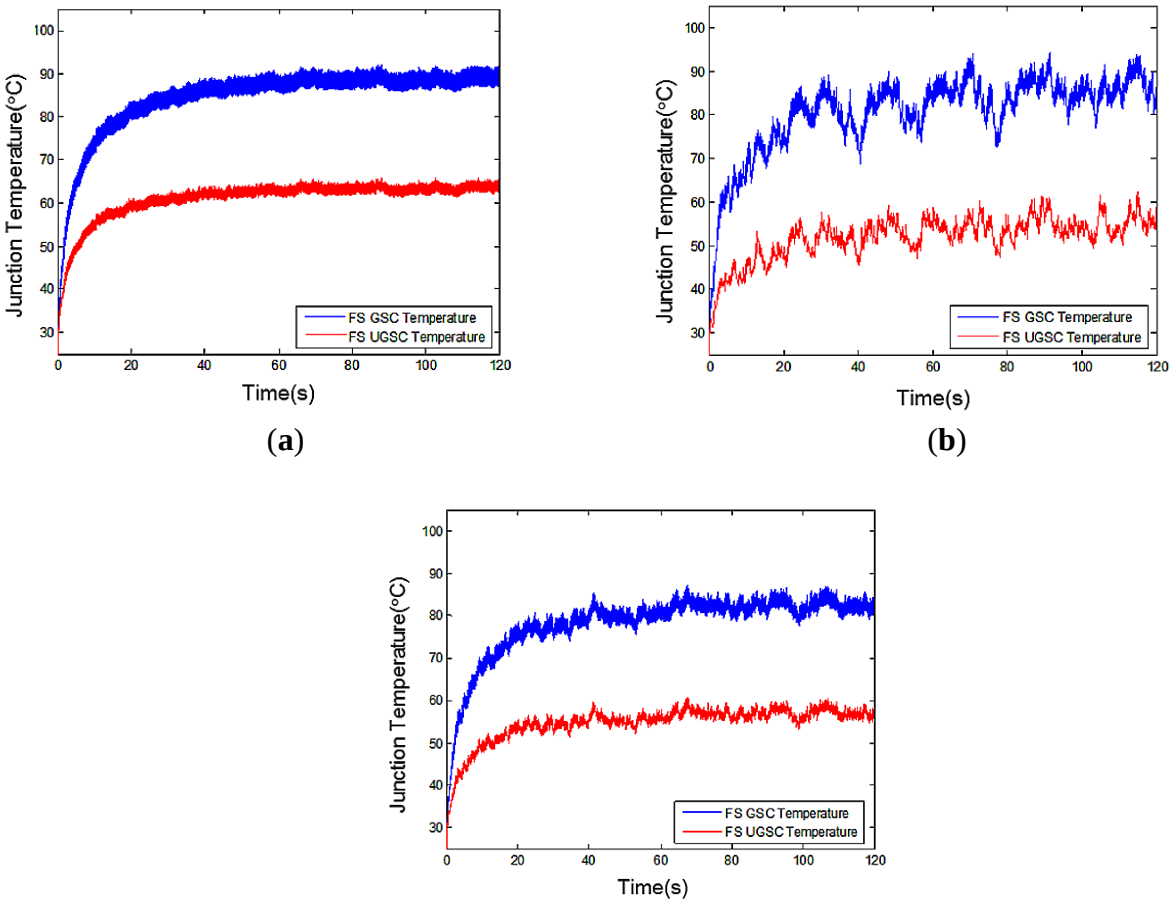

Figure 12. Temperature profile of FS based PECs with (**a**) conventional fixed DC link voltage; dynamic DC link (**b**) without and (**c**) switching frequency adaption schemes in generator side (GS) and utility grid side (UGS).

Temperature fluctuations, for variable DC link operation, are higher for the grid side converter devices, due to the distorted DC link voltage and current injection. In fact, the mean temperature is approximately 25 °C lower than generator side converter which means the power modules will experience higher thermal stress caused by wind variations. Compared to FS topology, mean and peak temperatures of the converter modules are greater and more fluctuated for both generator and grid sides of PS topology as seen in Figure 13a–c. Maximum temperature fluctuation is approximately 12 °C at t = 80 s. Also, when frequency control algorithm applied, mean temperature is reached 92 °C.

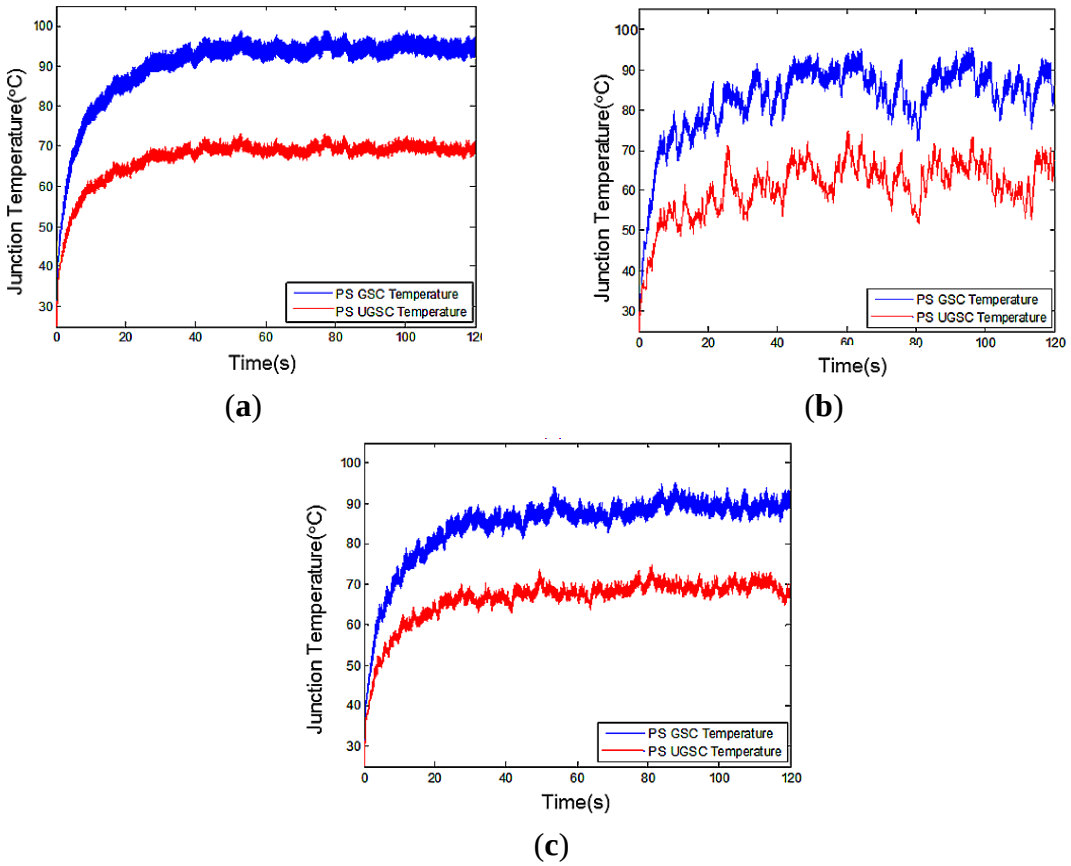

Figure 13. Temperature Profile of PS based PECs with (**a**) conventional fixed DC link voltage; dynamic DC link (**b**) without and (**c**) switching frequency adaption schemes in GS and UGS.

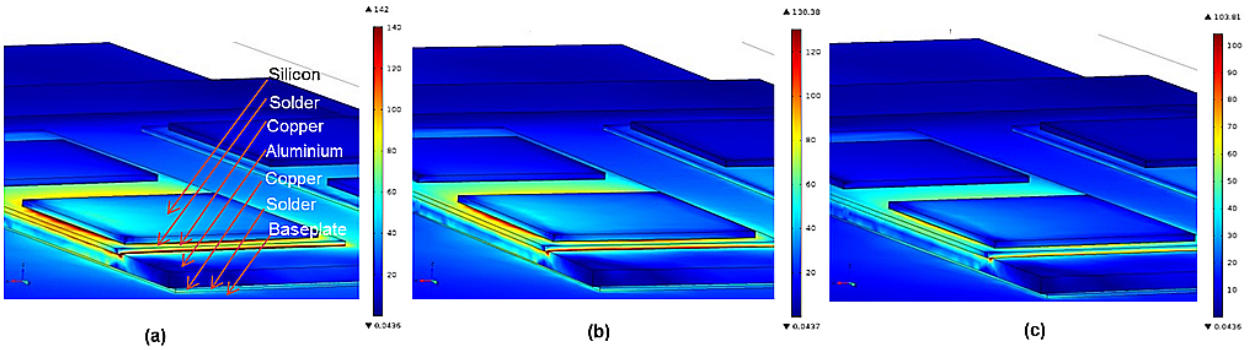

Figure 14. Surface von Mises stress for FS based BTB converter's generator side power module with (**a**) fixed DC link; (**b**) dynamic DC link without and (**c**) with switching frequency adaption.

The temperature fluctuation however is reduced by 9 °C which would reflect on the thermal stress induced during the operation. Similar to the FS converter topology, higher fluctuation (~15 °C) and lower mean junction temperature (~70 °C) profile were estimated, on the GSC.

3.3. Thermo-Mechanical Performance of Proposed Model

As a case study, FS generator side converters' power loss profiles of each three of the topological models were applied on top of the chips within FE analysis for obtaining the thermo-mechanical performances. Due to computational speed limitation in FEM, step time of loss profile was resampled into 5 ms range. Power losses were scaled by 1/12 factor; then were applied individually as boundary heat source on the each top surface of the silicon chip layer. This approach made it possible to locate thermal stress caused by thermo-coupling heat effect across neighbour chips located on each substrate. Von Mises stress which occurred due to the power loss profile extracted from each topological operating approach are shown in Figure 14.

It can be commented that the most stressed regions are the solder of silicon and copper of baseplate layers. The maximum von Mises stress is estimated at the edges of copper layer as 142 MPa for the fixed DC link operation as shown in Figure 14a. On the other hand, it is possible to reduce it around 130 MPa with dynamic DC link operation as depicted in Figure 14b. The performance of the proposed model in terms of maximum stress is also shown in Figure 14c. Compared to dynamic DC link mode, approximately 27 MPa stress deduction was attained. The maximum stress was reduced approximately to 103 MPa which is lower than the yield strength of the copper [31]. Stress across silicon layer edges and baseplate is reduced in overall, especially around solder of neighbour substrates compared to dynamic DC link approach. First principle stress analyses are shown in Figure 15a–c for each topology. Mostly effected regions are middle edge of the silicon and aluminium ceramic layers.

Proposed method showed better performance with total difference as lower as 36 MPa compare to the static and dynamic DC link operations. Total principal stress can be estimated as 56.6 MPa. Although dynamic DC link operation has lower mean junction temperature profile, thermal stress distribution is worse due its highly fluctuated characteristics, compared to proposed driving scheme.

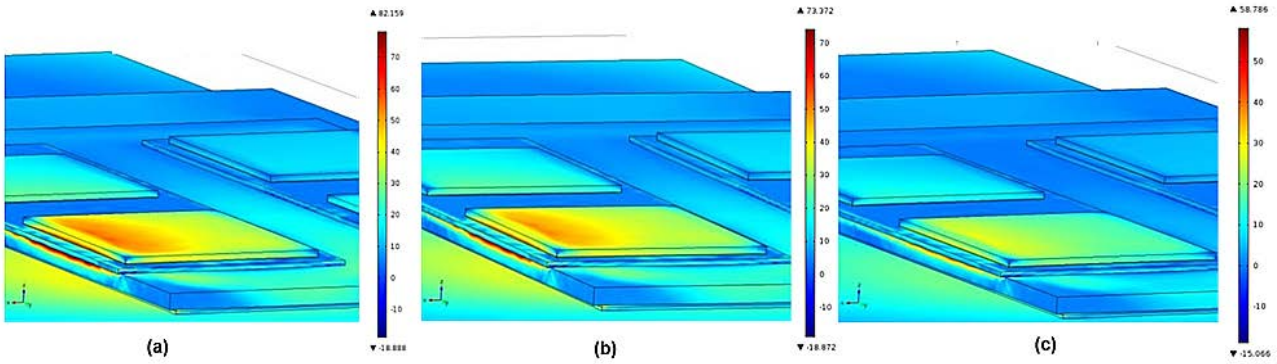

Figure 15. Surface first principle stress for FS based back-to-back (BTB) converter's generator side power module with (**a**) fixed DC link; (**b**) dynamic DC link without and (**c**) with switching frequency adaption.

Total power losses with respect to mean and temperature fluctuations and stress for both FS and PS schemes are shown in Figure 16. It is seen that the proposed scheme showed better performance for the FS based wind energy system. Mean junction temperatures are approximately lowered by 8 °C compared to the static DC link system for both GSC and UGSC. Temperature fluctuation is also decreased by means of 50% compare to the variable DC link operation which will be the major benefit for stress deduction. Although the instantaneous power losses at peak point are decreased by 20% in DFIG system, this deduction did not reflect on mean junction temperature and maximum stress (~7 MPa in GSC, ~10 MPa in UGSC) since the power absorption during sub-synchronous mode increase thermal cycling, unlike in FS topology. Despite of the highly cycling thermal profile, 5 °C mean junction temperature deduction is established compared to the conventional topology for both side converters of the PS based wind system model.

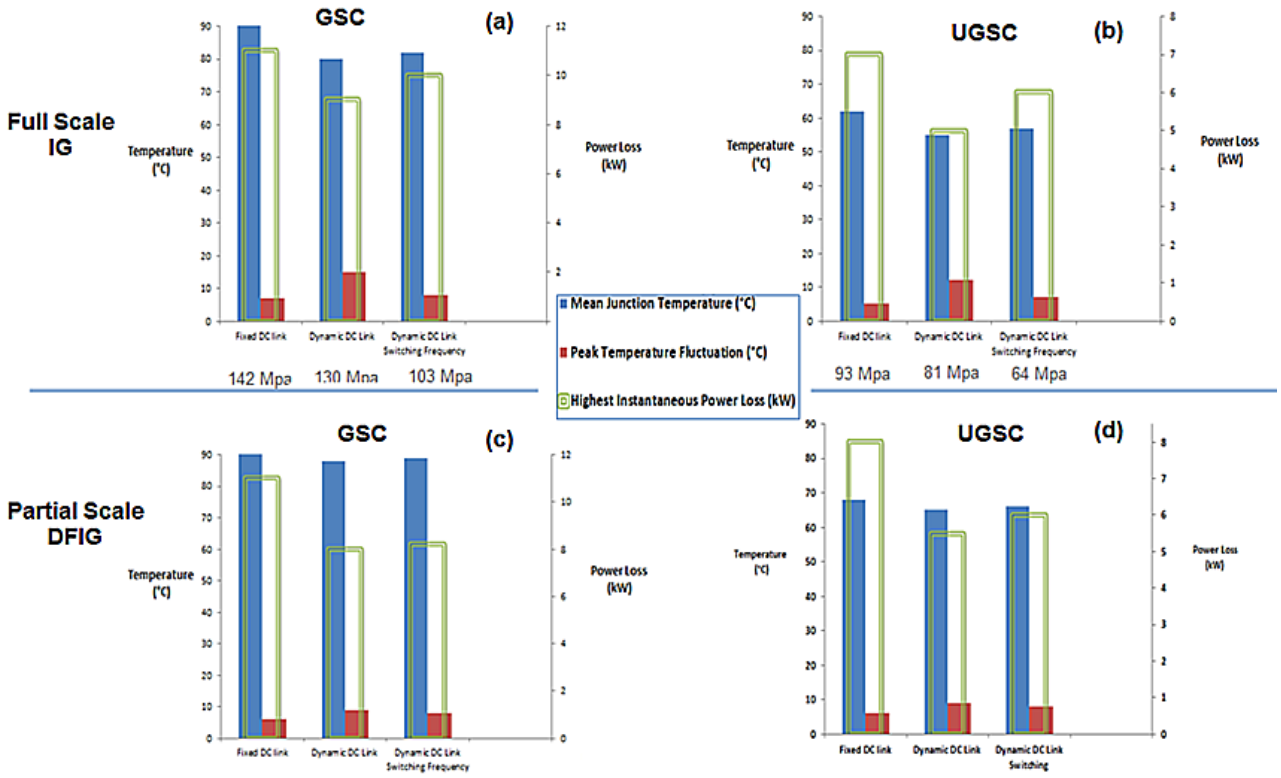

Figure 16. Overall thermo-mechanical and electro-thermal for (**a**,**c**) generator and (**b**,**d**) grid side power modules on FS and on PS doubly fed induction generator (DFIG) based BTB PECs.

4. Conclusions

A model based solution to minimise thermal effects and the induced stress of PECs was demonstrated in this paper. Promising results were achieved by optimising switching frequency of

PECs within dynamic DC link voltages for wind energy applications. The proposed adaptive switching driving scheme managed to control the total power losses of a two level back-to-back converter platform used in full scale (FS) and doubly fed induction generator (DFIG) based partial scale (PS) wind systems. Moreover, the IGBT junction's mean temperature and the induced stress were eliminated and kept within acceptable levels, which in turn maximise the life cycle of such PECs. With the proposed approach, "the total temperature fluctuation were notably reduced; for FSIG by 12 °C, DFIG by 5 °C. Such temperature reduction leads to a total stress decrease by about 27 MPa. The drawbacks associated with the proposed model are related to its complexity, possible current and voltage fluctuations which may cause increase to the total harmonic distortion fed into the utility grid.

Acknowledgments

This work is part of a PhD research funded by a scholarship from Manchester Metropolitan University.

Author Contributions

All authors contributed equally to the research described in this work. C.B. and A.A. conceived and designed the experiments. C.B. and A.A. performed the experiments and analyzed the data; C.B. wrote the paper.

Conflicts of Interest

The authors declare no conflict of interest.

References

1. Blaabjerg, F.; Liserre, M.; Ma, K. Power Electronics Converters for Wind Turbine Systems. *IEEE Trans. Ind. Appl.* **2012**, *48*, 708–719.
2. Zhou, D.; Blaabjerg, F.; Lau, M.; Tonnes, M. Thermal Cycling Overview of Multi-Megawatt Two-Level Wind Power Converter at Full Grid Code Operation. *IEEJ J. Ind. Appl.* **2013**, *2*, 173–182.
3. Ensslin, C.; Durstewitz, M.; Hahn, B.; Lange, B.; Rohrig, K. *German Wind Energy Report 2008*. Available online: http://windmonitor.iwes.fraunhofer.de/img/Wind_energy_report_2008.pdf (accessed on 17 July 2015).
4. Lu, H.; Bailey, C.; Yin, C. Design for reliability of power electronics modules. *Microelectron. Reliab.* **2009**, *49*, 1250–1255.
5. Darwish, A.M.; Bayba, A.; Hung, H.A. FET Gate Length Impact on Reliability. In Proceedings of the IEEE/MTT-S International Microwave Symposium, Honolulu, HI, USA, 3–8 June 2007; pp. 311–314.
6. Vermeersch, B.; de Mey, G. A Fixed-Angle Heat Spreading Model for Dynamic Thermal Characterization of Rear-Cooled Substrates. In Proceedings of the Twenty Third Annual IEEE Semiconductor Thermal Measurement and Management Symposium, San Jose, CA, USA, 18–22 March 2007; pp. 95–101.

7. Janicki, M.; de Mey, G.; Napieralski, A. Transient thermal analysis of multilayered structures using Green's functions. *Microelectron. Reliab.* **2002**, *42*, 1059–1064.
8. Swan, I.; Bryant, A.; Mawby, P. Fast Thermal Models for Power Device Packaging. In Proceedings of the IEEE Industry Applications Society Annual Meeting, Edmonton, AB, Canada, 5–9 October 2008; pp. 1–8.
9. Wu, J.; Zhou, L.; Du, X.; Sun, P. Junction Temperature Prediction of IGBT Power Module Based on BP Neural Network. *J. Electr. Eng. Technol.* **2014**, *9*, 970–977.
10. Skuriat, R.; Johnson, C.M. Thermal performance of baseplate and direct substrate cooled power modules. In Proceedings of the 4th IET Conference on Power Electronics, Machines and Drives, York, UK, 2–4 April 2008; pp. 548–552.
11. Huang, H.; Bryant, A.T.; Mawby, P.A. Electro-thermal modelling of three phase inverter. In Proceedings of the 2011—14th European Conference on Power Electronics and Applications, Birmingham, UK, 30 August–1 September 2011; pp. 1–7.
12. Ma, K.; Blaabjerg, F. The Impact of Power Switching Devices on the Thermal Performance of a 10 MW Wind Power NPC Converter. *Energies* **2012**, *5*, 2559–2577.
13. Ma, K.; Blaabjerg, F. Multilevel converters for 10 MW Wind Turbines. In Proceedings of the 2011—14th European Conference on Power Electronics and Applications, Birmingham, UK, 30 August–1 September 2011; pp. 1–10.
14. Senturk, O.S.; Helle, L.; Munk-Nielsen, S.; Rodriguez, P.; Teodorescu, R. Converter Structure-Based Power Loss and Static Thermal Modeling of the Press-Pack IGBT Three-Level ANPC VSC Applied to Multi-MW Wind Turbines. *IEEE Trans. Ind. Appl.* **2011**, *47*, 2505–2515.
15. Blaabjerg, F.; Ma, K.; Zhou, D. Power electronics and reliability in renewable energy systems. In Proceedings of the IEEE International Symposium on Industrial Electronics, Hangzhou, China, 28–31 May 2012; pp. 19–30.
16. Lee, J.S.; Lee, K.B. Variable DC-Link Voltage Algorithm with a Wide Range of Maximum Power Point Tracking for a Two-String PV System. *Energies* **2013**, *6*, 58–78.
17. Gao, F.; Li, D.; Loh, P.C.; Tang, Y.; Wang, P. Indirect dc-link voltage control of two-stage single-phase PV inverter. In Proceedings of the IEEE Energy Conversion Congress and Exposition, San Jose, CA, USA, 20–24 September 2009; pp. 1166–1172.
18. Zou, Y.; Elbuluk, M.; Sozer, Y. Stability analysis of maximum power point tracking (MPPT) method in wind power systems. In Proceedings of the IEEE Industry Applications Society Annual Meeting (IAS), Orlando, FL, USA, 9–13 October 2011; pp. 1–8.
19. Han, K.; Chen, G. A novel control strategy of wind turbine MPPT implementation for direct-drive PMSG wind generation imitation platform. In Proceedings of the Power Electronics and Motion Control Conference, IPEMC 6th Int IEEE, Wuhan, China, 17–20 May 2009; pp. 2255–2259.
20. El-Sousy, F.F.M.; Orabi, M.; Godah, H. Maximum Power Point Tracking Control Scheme for Grid Connected Variable Speed Wind Driven Self-Excited Induction Generator. *J. Power Electron.* **2006**, *6*, 52–66.
21. Bekakra, Y.; Attous, D.B. DFIG sliding mode control fed by back-to-back PWM converter with DC-link voltage control for variable speed wind turbine. *Front Energy* **2014**, *8*, 345–354.
22. Dayaratne, U.I.; Tennakoon, S.B.; Shammas, N.Y.A.; Knight, J.S. Investigation of variable DC link voltage operation of a PMSG based wind turbine with fully rated converters at steady state.

In Proceedings of the 14th European Conference on Power Electronics and Applications (EPE), Birmingham, UK, 30 August–1 September 2011; pp. 1–10.

23. Yu, C.Y.; Tamura, J.; Lorenz, R.D. Control method for calculating optimum DC bus voltage to improve drive system efficiency in variable DC bus drive systems. In Proceedings of the IEEE Energy Conversion Congress and Exposition (ECCE), Raleigh, NC, USA, 15–20 September 2012; pp. 2992–2999.
24. Pei, X.; Kang, Y.; Chen, J. Analysis and calculation of DC-link current and voltage ripple for three-phase inverter with unbalanced loads. In Proceedings of the Twenty-Ninth Annual IEEE Applied Power Electronics Conference and Exposition, Fort Worth, TX, USA, 19–20 March 2014; pp. 1565–1572.
25. Lemmens, J.; Driesen, J.; Vanassche, P. Thermal management in traction applications as a constraint optimal control problem. In Proceedings of the IEEE Vehicle Power and Propulsion Conference (VPPC), Seoul, South Korea, 9–12 October 2012; pp. 36–41.
26. Andresen, M.; Liserre, M. Impact of active thermal management on power electronics design. *Microelectron. Reliab.* **2014**, *54*, 1935–1939.
27. Ma, K.; Blaabjerg, F. Reliability-cost models for the power switching devices of wind power converters. In Proceedings of the 3rd IEEE International Symposium on Power Electronics for Distributed Generation Systems (PEDG), Aalborg, Denmark, 25–28 June 2012; pp. 820–827.
28. Ma, K.; Bahman, A.S.; Beczkowski, S.; Blaabjerg, F. Complete Loss and Thermal Model of Power Semiconductors Including Device Rating Information. *IEEE Trans. Power Electron.* **2015**, *5*, 2556–2569.
29. Kuhn, H.; Mertens, A. On-line junction temperature measurement of IGBTs based on temperature sensitive electrical parameters. In Proceedings of the 13th European Conference on Power Electronics and Applications, Barcelona, Spanish, 8–10 September 2009, pp. 1–10.
30. Mysore, K.; Subbarayan, G.; Gupta, V.; Zhang, R. Constitutive and Aging Behavior of Sn3.0Ag0.5Cu Solder Alloy. *IEEE Trans. Electron. Packag. Manuf.* **2009**, *32*, 221–232.
31. Liu, Y. *Power Electronic Packaging: Design, Assembly Process, Reliability and Modeling*; Springer Science & Business Media: New York, NY, USA, 2012; pp. 3–7.
32. Online Materials Information Resource. Available online: http://www.matweb.com/ (accessed on 15 July 2015).
33. Shaoyong, Y; Bryant, A.; Mawby, P.; Dawei, X.; Li, R.; Tavner, P. An Industry-Based Survey of Reliability in Power Electronic Converters. *IEEE Trans. Ind. Appl.* **2011**, *47*, 1441–1451.
34. Drofenik, U.; Cottet, D.; Müsing, A.; Meyer, J.; Kolar, J.W. Modelling the Thermal Coupling between Internal Power Semiconductor Dies of a Water-Cooled 3300 V/1200 A HiPak IGBT Module. In Proceedings of the Conference for Power Electronics, Intelligent Motion, Power Quality, Nuremberg, Germany, 22–24 May 2007; pp. 22–24.
35. Ye, H.; Lin, M.; Basaran, C. Failure modes and FEM analysis of power electronic packaging. *Finite Elem. Anal. Des.* **2002**, *38*, 601–612.
36. Xu, L.; Liu, Y.; Liu, S. Modeling and simulation of power electronic modules with microchannel coolers for thermo-mechanical performance. *Microelectron. Reliab.* **2014**, *54*, 2824–2835.
37. Anand, L. Constitutive Equations for the Rate-Dependent Deformation of Metals at Elevated Temperatures. *J. Eng. Mater. Technol.* **1982**, *104*, 12–17.

38. Mohan, N. *Advanced Electric Drives: Analysis, Control, and Modeling Using MATLAB/Simulink*; John Wiley & Sons: Hoboken, NJ, USA, 2014; pp. 28–37.

39. Kaźmierkowski, M.P.; Krishnan, R.; Blaabjerg, F. *Control in Power Electronics: Selected Problems*; Academic Press: Amsterdam, NY, USA, 2002; pp. 434–435.